CAVITATION ESTIMATES BY ORBIT PREDICTION OF A JOURNAL BEARING - FINITE ELEMENT MODELLING AND EXPERIMENTAL STUDIES

C.K. Christiansen[1]*, P. Klit[1], J.H. Walther[1,2], A. Vølund[3]

[1]Department of Mechanical Engineering, Technical University of Denmark, Nils Koppels Allé, bld. 404, 2800 Kgs. Lyngby, Denmark.
[2]Computational Science & Engineering Laboratory, ETH, Clausiusstrasse 33, Zürich, CH-8092, Switzerland.
[3]MAN Diesel & Turbo, Teglholmsgade 41, 2450 Copenhagen SV, Denmark.

ABSTRACT

The paper presents a two-sided approach to establish understanding of the cavitation phenomenon in dynamically loaded journal bearings, more specifically the engine bearings of large two-stroke marine diesel engines. One disadvantage of the journal bearing is the converging-diverging geometry making it prone to cavitation which again affects the load carrying capacity of the bearing. In combustion engines the journal bearing plays a vital role especially as main and crosshead bearings transmitting the combustion forces. Those forces vary highly during one combustion cycle which is further influencing the load carrying capacity and ultimately the chances of fatal shaft-sleeve contact. By solving Reynolds equation numerically using finite elements and incorporating a cavitation algorithm, the dynamic coefficients can be used to establish the journal orbit for a given bearing and load pattern. Validation of the results is done against the Ruston and Hornsby 6VEB-X Mk III engine. Besides the numerical investigations a cavitation test rig has been developed. With this rig it is possible to generate cavitation under controlled conditions in terms of load/eccentricity and rotational speed. The development of cavitation in time in terms of position and distribution can be visually recorded.

Keywords: Cavitation, journal bearing, Finite Element, journal orbit, test rig.

*Corresponding author: Christian Christiansen (chkch@mek.dtu.dk).

INTRODUCTION

Journal bearings are used in a wide range of applications due to their simplicity and derived low cost but also a reasonable load carrying capacity. On the other hand, one of the most often mentioned disadvantages of the journal bearing is the converging-diverging geometry making it prone to cavitation. The general concepts of bearing cavitation are outlined in the thorough review of Dowson and Taylor [1]. In short two types of cavitation exists; gaseous cavitation and vaporous cavitation. Gaseous cavitation occurs from the release of entrained air in the lubricant being released at pressures equal to, or below, the saturation pressure of the lubricant. Vaporous cavitation on the other hand, is governed by the vapour pressure such that the lubricant starts boiling even at low temperatures, when the pressure drops below the vapour pressure. This phenomenon is what is known from a very broad range of areas; ship propellers being eroded on the surface, medical care and cleaning applications by the formed shock waves etc. [2].

For typical lubricants the saturation pressure is just sub-atmospheric whereas the vapour pressure is much closer to zero. Hence, the gaseous cavitation will occur first and work as a limiter, such that vaporous cavitation is very unlikely to occur for statically loaded journal bearings. This is not the case for a dynamically loaded bearing [1]. Here bubbles are forming in the boiling lubricant and the vaporous cavitation is characterised by the bubbles collapsing violently, blasting the surface yielding pressures in the order of

10^8 **Pa** [3]. While the gaseous cavitation process itself is rather harmless compared to the vaporous one, the formation and/or concentration of released bubbles reduces the load carrying capacity locally, due to a decreased filling ratio, i.e. ratio between lubricant and vapour.

For dynamically loaded bearings as found in reciprocating machinery this reduction of load carrying capacity is of great importance. The reduction might lead to fatal journal-bearing housing contact, which will be revealed in a journal orbit plot. Booker used the mobility method in 1965 and 1971 to predict the orbit [4,5]. Adapting the concepts from stability and vibration analysis, Lund and Thomsen found that the dynamic coefficients revealed the behaviour of a statically loaded bearing using finite differences [6]. Klit and Lund developed a finite element formulation in the 1980's for obtaining the dynamic coefficients at an instant in time for a statically loaded bearing [7]. With very little effort these coefficients could be integrated in time to predict an entire orbit as shown with analytical coefficients in an unpublished paper by Klit and Vølund [8]. For evaluating new methods, the Ruston and Hornsby 6VEB-X Mk III 4-stroke diesel engine has become a widespread benchmark case over the years [5,9,10].

Although the orbit has been available for a journal bearing for 50 years with the mobility method, this method is limited to ideal bearings without grooves and other irregularities. The present work will show the application of the finite element method to obtain the journal orbit for a dynamically loaded journal bearing, and hence allow for a complex bearing design including grooves and inlets of various geometries by using the adaptability of the finite element method. Within the finite element model various cavitation models can be applied. For this work the half-Sommerfeld model is used for simplicity.

THEORY

Due to the non-linear relations between forces and journal position in Reynolds equation an iterative procedure is required to obtain the journal orbit corresponding to a complete load cycle. Based on a sequence of local force equilibria, a time-integration scheme sums up the contributions, yielding the journal orbit.

The theory is to a large extent similar to the one used by Klit and Lund [8]. However, where they assumed no whirling, it is included in the present work to account for the dynamic effects. The final equations will enable the prediction of the journal orbit for a sequence of loads, given at e.g. 2° of crank rotation.

The pressure distribution in the bearing is described by Reynolds equation. This work uses the non-dimensional version indicated by the bar notation:

$$\frac{\partial}{\partial \theta}\left(\bar{h}^3 \frac{\partial \bar{p}}{\partial \theta}\right) + \frac{\partial}{\partial \zeta}\left(\bar{h}^3 \frac{\partial \bar{p}}{\partial \zeta}\right) = \frac{\partial \bar{h}}{\partial \theta} + \frac{2\nu}{\omega}\frac{d\bar{h}}{d\tau} \qquad (1)$$

With $\boldsymbol{\theta}$ being the circumferential coordinate (from zero film thickness), $\bar{h}$ is film thickness, $\bar{p}$ is pressure, $\boldsymbol{\zeta}$ is axial coordinate, $\boldsymbol{\nu}$ is a parameter of unit **rad/s**, $\boldsymbol{\omega}$ is angular velocity (of crankshaft) and $\boldsymbol{\tau}$ is time. The film thickness can be expressed as:
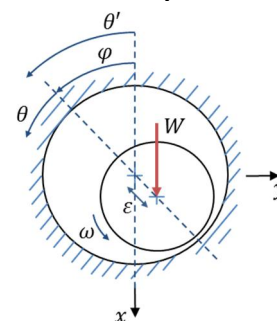
Figure 1. The journal bearing geometry in the global coordinate system $(\boldsymbol{x}, \boldsymbol{y})$. $\boldsymbol{\theta}'$ is the global film coordinate, $\boldsymbol{\theta}$ the local film coordinate, $\boldsymbol{\varphi}$ is the attitude angle, $\boldsymbol{W}$ is imposed load, $\boldsymbol{\varepsilon}$ is eccentricity, $\boldsymbol{\omega}$ is angular velocity.

$$\bar{h} = 1 + \varepsilon \cos \theta = 1 + \varepsilon \cos(\theta' - \varphi)$$
$$= 1 + \bar{x} \cos \theta' + \bar{y} \sin \theta' \quad (2)$$

Where θ' is the film angle from the vertical axis and φ is the attitude angle and $\bar{x}, \bar{y}$ can be expressed on the form $\bar{x} = \bar{x}_0 + \Delta\bar{x}$, i.e. a stationary term and a perturbation.

Klit and Lund used the perturbation method to analyse the influence of shaft position $(\Delta\bar{x}, \Delta\bar{y})$ and velocity $(\Delta\dot{\bar{x}}, \Delta\dot{\bar{y}})$ on the dynamic properties of the shaft. Define a perturbed pressure:

$$\bar{p} = \bar{p}_0 + \Delta\bar{x}\bar{p}_1 + \Delta\bar{y}\bar{p}_2 + \Delta\dot{\bar{x}}\,\bar{p}_3 + \Delta\dot{\bar{y}}\,\bar{p}_4 \quad (3)$$

With Eq. (3) five functionals can be derived. These functionals serve as the basis for the finite element equations for solving $\bar{p}_i, i = 0, 1, \ldots, 4$. Considering one element the equations become:

$$-\int_A \left(-\bar{h}_0^3 \left[\left(\frac{\partial N}{\partial \theta}\right)^T \left(\frac{\partial N}{\partial \theta}\right) + \left(\frac{\partial N}{\partial \zeta}\right)^T \left(\frac{\partial N}{\partial \zeta}\right)\right] \bar{p}_i + RHS\right) dA = 0 \quad (4a)$$

RHS =

$$\begin{cases}
\left[\bar{h}_o + \frac{2\nu}{\omega}(\dot{\bar{x}}_0 \sin \theta' - \dot{\bar{y}}_0 \cos \theta')\right]\frac{\partial N^T}{\partial \theta} & \text{for } \bar{p}_0 \\[6pt]
-3\bar{h}_o^2 \cos \theta' \left[\left(\frac{\partial N}{\partial \theta}\right)^T \left(\frac{\partial N}{\partial \theta}\right) + \left(\frac{\partial N}{\partial \zeta}\right)^T \left(\frac{\partial N}{\partial \zeta}\right)\right]\bar{p}_0 \\[4pt]
\quad + \cos \theta' \left(\frac{\partial N}{\partial \theta}\right)^T & \text{for } \bar{p}_1 \\[6pt]
-3\bar{h}_o^2 \cos \theta' \left[\left(\frac{\partial N}{\partial \theta}\right)^T \left(\frac{\partial N}{\partial \theta}\right) + \left(\frac{\partial N}{\partial \zeta}\right)^T \left(\frac{\partial N}{\partial \zeta}\right)\right]\bar{p}_0 \\[4pt]
\quad + \sin \theta' \left(\frac{\partial N}{\partial \theta}\right)^T & \text{for } \bar{p}_2 \\[6pt]
\frac{2\nu}{\omega} \sin \theta' \frac{\partial N^T}{\partial \theta} & \text{for } \bar{p}_3 \\[6pt]
-\frac{2\nu}{\omega} \cos \theta' \frac{\partial N^T}{\partial \theta} & \text{for } \bar{p}_4
\end{cases}$$
$$(4b)$$

Where N is the vector containing the element shape functions. The resulting system of equations is fast to solve as the stiffness matrix on the left hand side only needs to be assembled once for each time step (Eq. 4a). The term RHS specifies the five different right hand sides in the equation system.

After obtaining $\bar{p}_i$ the load carrying capacity and dynamic coefficients can be found from:

$$\left.\begin{array}{l}f_x \\ f_y\end{array}\right\} = \frac{6\pi}{L/D} \int_0^{L/D} \int_0^{2\pi} \bar{p}_0 \begin{Bmatrix} -\cos \theta' \\ -\sin \theta' \end{Bmatrix} d\theta d\zeta \quad (5a)$$

$$\left.\begin{array}{l}\bar{K}_{xx} \\ \bar{K}_{yx}\end{array}\right\} = \frac{6\pi}{L/D} \int_0^{L/D} \int_0^{2\pi} \bar{p}_1 \begin{Bmatrix} -\cos \theta' \\ -\sin \theta' \end{Bmatrix} d\theta d\zeta \quad (5b)$$

$$\left.\begin{array}{l}\bar{B}_{xx} \\ \bar{B}_{yx}\end{array}\right\} = \frac{6\pi}{L/D} \int_0^{L/D} \int_0^{2\pi} \bar{p}_3 \begin{Bmatrix} -\cos \theta' \\ -\sin \theta' \end{Bmatrix} d\theta d\zeta \quad (5c)$$

Here L/D is the length/diameter ratio of the bearing. Using $\bar{p}_2$ and $\bar{p}_4$, respectively, yields the stiffness $\bar{K}_{xy}$ and $\bar{K}_{yy}$ and damping $\bar{B}_{xy}$ and $\bar{B}_{yy}$. For the journal orbit, only the damping coefficients are required. For the imposed load W_x, W_y in step k, the journal velocity is found from solving Eq. (6) in iterations numerated by j.

$$\begin{bmatrix} \bar{B}_{xx_j} & \bar{B}_{xy_j} \\ \bar{B}_{yx_j} & \bar{B}_{yy_j} \end{bmatrix} \begin{Bmatrix} \Delta\dot{\bar{x}}_j \\ \Delta\dot{\bar{y}}_j \end{Bmatrix} = \begin{Bmatrix} \bar{W}_{x_k} - f_{x_j} \\ \bar{W}_{y_k} - f_{y_j} \end{Bmatrix} \quad (6)$$

Please, note that formally $f_{i_j} = f_{i_j}(\bar{x}_k, \bar{y}_k, \dot{\bar{x}}_{k_j}, \dot{\bar{y}}_{k_j})$. Now the new shaft velocity is:

$$\dot{\bar{x}}_{k_{j+1}} = \dot{\bar{x}}_{k_j} + \Delta\dot{\bar{x}}_j \quad (7a)$$
$$\dot{\bar{y}}_{k_{j+1}} = \dot{\bar{y}}_{k_j} + \Delta\dot{\bar{y}}_j \quad (7a)$$

The velocity is adjusted by solving Eqs. (4)-(7) iteratively. Let k designate the load step, the convergence criterion is then chosen as a norm of the type:

$$\frac{|W_{x_k} - f_{x_j}| + |W_{y_k} - f_{y_j}|}{|W_{x_k}| + |W_{y_k}|} < tol \simeq 10^{-5} \quad (8)$$

After convergence is obtained, a first-order forward Euler method is used to step forward in time to the imposition of load $k + 1$:

$$\bar{x}_{k+1} = \bar{x}_k + \Delta t \dot{\bar{x}}_k \quad (9a)$$
$$\bar{y}_{k+1} = \bar{y}_k + \Delta t \dot{\bar{y}}_k \quad (9b)$$

In this way the journal orbit after one load cycle is of course affected by the initial guess for the journal position and velocity. Going through the load cycle consecutively will lead to steady state, usually after a few cycles.

BENCHMARK CASE

As a validation case, the widely used Ruston and Hornsby 6VEB-X Mk III engine is used, see further [5,9]. Fig. 2 shows the setup adapted from [5]. The loads shown in Fig. 3 are given for one land of the connecting rod big end bearing (shown here with cubic interpolation from 10° crank rotation to 1°) which is having one circumferential groove. It is assumed the boundary conditions on this half-width bearing can be considered to be atmospheric pressure. The remaining used data are listed in Table 1.
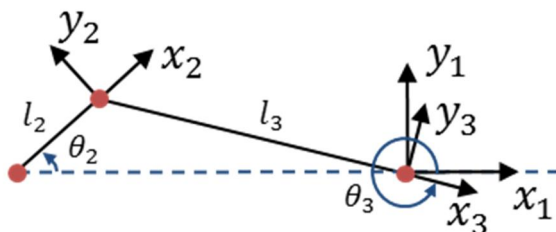
Figure 2. Geometry of crank rod-connecting rod assembly (redrawn from Booker, [5]).The coordinate systems 2 and 3 are following the crank and connecting rod, respectively, whereas the coordinate system 1 is aligned to the piston.

Table 1. Dimensions and properties of the Ruston and Hornsby 6VEB-X Mk III connecting rod bearing (from Booker, [5]).

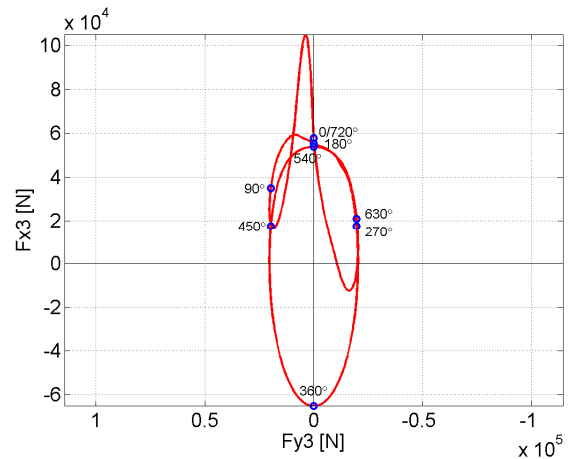| Parameter	Value
l_2	0.1841 m
l_3	0.7823 m
D	0.2032 m
L	0.0572 m
C	$82.55 \cdot 10^{-6}$ m
μ	0.015 Pa $\cdot$ s
RPM	300

Figure 3. Load diagram obtained from data by Booker, [5]. Cubic interpolation is applied from 10° crank rotation to 1°.

RESULTS

The main result is the direct benchmark between literature and the present work with regards to the journal orbit. Fig. 4 is the solution by Campbell et al from their review [9, Fig. 9b], where it is one of a dozen solutions computed from graphical, mobility and finite difference methods by various institutions as well as experimental results. The minimum film thickness is a key parameter of interest and found to be 5.5 µm at 277° after top dead centre (TDC). Campbell et al reports this to be in the interval 2.3 µm-12.9 µm and 270°-290°. The arbitrary initial guess requires as expected in Section 2, a number of consecutive runs of the load cycle. Using the bearing centre as initial location (($\bar{x}, \bar{y}$) = **(0,0)**), a stable orbit is found within two runs.

Fig. 5 shows the present work and qualitatively agreement is obtained. It is noted that the position of the indicated angles and the sharp turn seen between
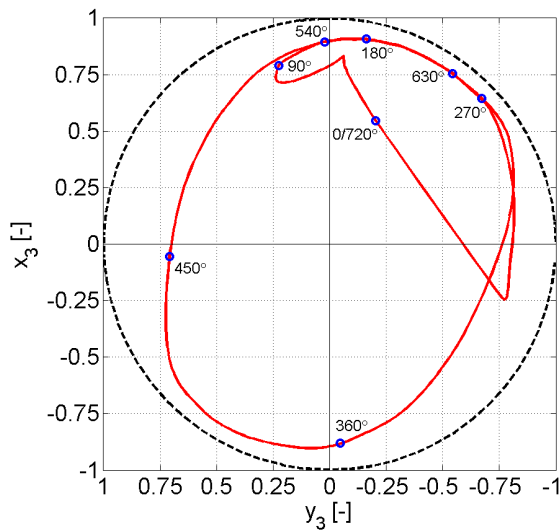
Figure 4. Journal orbit by Campbell et al (1967) made from the short bearing solution and the graphical method [9].
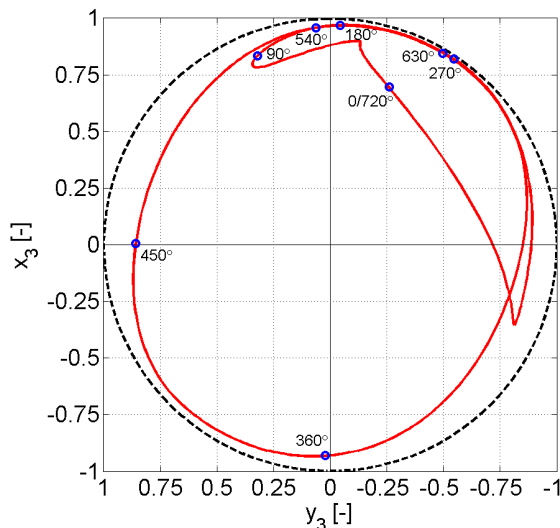

Figure 5. Journal orbit for present code with 60 x 16 elements.

630° and 720° is changing from computation to computation in the work of Campbell et al, such that the results contain some influence from the models used. The minimum film thickness of 0.8 µm is located at 275° after TDC. A mesh of 30 x 8 triangular elements is used and this seems to be sufficient to predict the nature of the orbit (very small changes occur with 45 x 12 or 60 x 16 elements). However, the minimum film thickness increases from 0.8 µm over 1.2 µm to 1.3 µm and changes location from 275° after TDC to 271° after TDC when increasing the

resolution. Unsurprisingly, it appears that the low-order element mimics the nature of the solution with few elements, but accurate values require a high number of elements.

With the journal orbit found, it is easy to calculate the volume of the cavitated areas from the local film thickness and hence obtain knowledge useful for the specification of the flow rates required for an inlet nozzle. From Fig. 6 and the principle of mass conservation the following relation can be established:
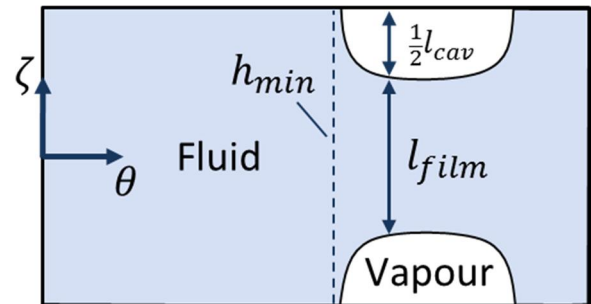

Figure 6. Sketch of two cavitated areas (symmetry around $\zeta = 0$) and their size due to mass conservation.

$$l_{cav} = L\left(1 - \frac{\bar{h}_{min}}{\bar{h}_{film}}\right) \qquad (10)$$

The cavitated volume is now simply the arc length times length times height, or in non-dimensional terms:

$$\bar{v}_{cav} = \Delta\theta\zeta(\bar{h}_{film} - \bar{h}_{min}) \qquad (11)$$

The dimensional expression is thus:

$$v_{cav} = \bar{v}_{cav} \cdot R^2 C \qquad (12)$$

The cavitated volumes are plotted as a function of the crank ankle degree (CAD) for one combustion cycle in Fig. 7. Here on the other hand, a higher resolution for the mesh is required to eliminate fluctuations in the volumes due to abrupt changes in what element, and thus film height, is seen as cavitated or not. Recall, that one element spans over 12° of the bearing circumference

for the coarse mesh and only 6° for the fine mesh. Fig. 7 will serve as tool for pinpointing the angular position(s) where improved filling might influence the dynamic properties and hence journal orbit significantly. Due to the application of the half-Sommerfeld model, the *full* film history is not known. Areas of full film are treated with 100% load carrying capacity, while cavitated areas have no load carrying capacity. Thus, the angular difference α between the starting point of film rupture for half-Sommerfeld (180°) and a complete cavitation model - e.g. by applying Reynolds boundary conditions $d p / d \vec{n} = 0$, where $\vec{n}$ is the normal vector to the film front - (rupture at 180°+ α), is not accounted for with a weight between 0 and 1. In other words filling of cavitated areas occurs infinitely fast in this work and no intermediate stage exists.
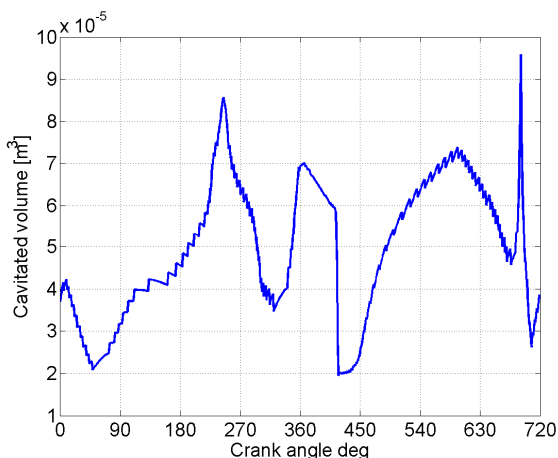
Another way to interpret the journal orbit of Fig. 5 is given in Fig. 8. Here cavitated zone is plotted in blue and the direction of the imposed load of Fig. 3 is plotted in red. It is interesting to see the dynamics of the bearing coupled with the imposed load. Notice the first large change in load after a few degrees of crankshaft rotation is not shown as dramatic as the rapid change in magnitude and sign occurring around 270° and around 450°. The sharp turn between 630° and 720° is also recognised on the plot, showing how the rapid change in load direction dictates a very rapid change, such that e.g. $\theta = \pi/2$ undergoes a transition from cavitated to non-cavitated and back to cavitated within a short period of time. This is also represented by the spike in Fig. 7.

CAVITATION TEST RIG

To validate the numerical findings a test rig has been developed and manufactured. Entitled Cavitation Test Rig (CTR) the idea is to monitor the formation of cavitation tongues, the so-called striations inside an acrylic bearing, see Fig. 9. The bearing is supported by a steel sleeve including an inspection slot. The 3 degrees of freedom necessary to follow a locus curve are ensured by mounting the shaft on a hinged table, whereas the bearing is stationary. The shaft is loaded with a hydraulic cylinder capable of both static and dynamic loads.

In Fig. 10 a photo of the preliminary operation is shown for a static load and the formation of three striations is clearly visible. This is meant as an example demonstration of the ability to generate cavitation in desired locations for visual studies. The numerical results demonstrated in Fig. 5 would only be reproducible with the data logging equipment illustrated in Fig. 9.

Figure 7. Cavitated volumes as function of CAD for present code with 60 x 16 elements.

Figure 8. Map of cavitated area as function of CAD for present code with 60 x 16 elements.
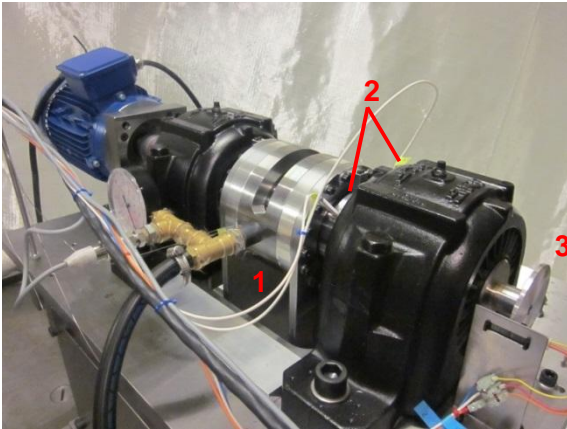
Figure 9. Cavitation test rig (CTR) shown with oil inlet (1), distance sensors (2) and tachometer (3). Load arrangement is hidden below the set-up. The inspecting slot is visible just above the inlet hose with the manometer.
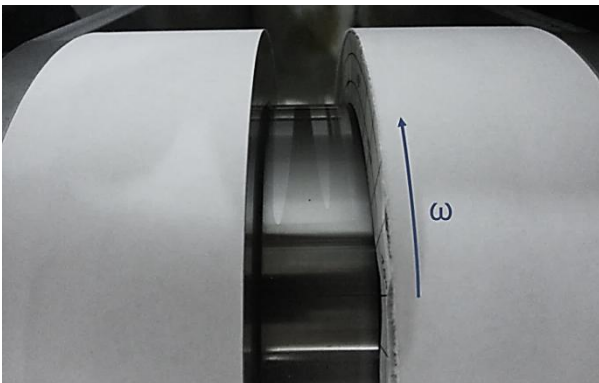

Figure 10. Example on cavitation taking the form of tongues or 'striations' seen in white.

CONCLUSIONS

The crude half-Sommerfeld model assumption proves sufficient to mimic the behaviour of a journal bearing exposed to a dynamic load cycle, when comparing to a classical benchmark case of the literature.

The used low-order finite element scheme captures the orbit in a qualitative way with few elements, but quantitatively results needs a fine mesh.

From the predicted journal orbit the volume (and location) of the cavitated areas can be calculated, improving the basis for decision in terms of inlet nozzle and groove design.

A test rig for monitoring cavitation in a journal bearing under controlled conditions has been developed. The preliminary results obtained during run-in seem promising.

REFERENCES

1. D. Dowson, C.M. Taylor, Cavitation in Bearings. Ann. Rev. Fluid Mech. (11) (1979), pp. 35-66.
2. D. Lohse, Bubble Puzzles, Physics Today, February 2003, pp.36-41.
3. M.S. Plesset, R.B. Chapman, Collapse of an initially spherical vapour cavity in the neighbourhood of a solid boundary, J. Fluid Mech. (47), part 2, 1971, pp. 283-290.
4. J.F. Booker, Dynamically-Loaded Journal Bearings: Mobility Method of Solution, Transactions of the ASME, 1965, pp.537-546.
5. J.F. Booker, Dynamically-Loaded Journal Bearings: Numerical Application of the Mobility Method, Transactions of the ASME, 1971, pp.168-174.
6. J.W. Lund, K.K. Thomsen, A Calculation Method and Data for the Dynamic Coefficients of Oil-lubricated Journal Bearings, Topics in Fluid Film Bearing and Rotor Bearing System Design and Optimization, ASME publ., 1978, pp. 1-28.

7. P. Klit, J.W. Lund, Calculation of the Dynamic Coefficients of a Journal Bearing, Using a Variational Approach, Journal of Tribology, (108) 1986, pp.421-424.

8. P. Klit, A. Vølund, Shaft Center Orbit for Dynamically Loaded Journal Bearings, DTU Mechanical Engineering, 2000, (unpublished).

9. J. Campbell, P.P Love, F.A. Martin, S.O. Rafique, Bearings for Reciprocating Machinery: A Review of the Present State of Theoretical, Experimental and Service Knowledge, Proc Instn Mech Engrs 1967-68, (182), Part 3A, pp. 51-70.

10. J.D.C. McIvor, The Analysis of Dynamically Loaded Flexible Journal Bearings Using Higher-Order Finite Elements, PhD thesis, Kings College London, 1988.